Journal of Power Sources 195 (2010) 6637–6644

Contents lists available at ScienceDirect

Journal of Power Sources

journal homepage: www.elsevier.com/locate/jpowsour

Modeling of electrochemistry and steam–methane reforming performance for simulating pressurized solid oxide fuel cell stacks

Kurtis P. Recknagle*, Emily M. Ryan, Brian J. Koeppel, Lenna A. Mahoney, Moe A. Khaleel

Pacific Northwest National Laboratory, Richland, WA 99352, USA

ARTICLE INFO

Article history:
Received 26 February 2010
Received in revised form 7 April 2010
Accepted 8 April 2010
Available online 15 May 2010

Keywords:
Electrochemistry
Pressurized
DIR
SOFC
Performance
Modeling

ABSTRACT

This paper examines the electrochemical and direct internal steam–methane reforming performance of the solid oxide fuel cell when subjected to pressurization. Pressurized operation boosts the Nernst potential and decreases the activation polarization, both of which serve to increase cell voltage and power while lowering the heat load and operating temperature. A model considering the activation polarization in both the fuel and the air electrodes was adopted to address this effect on the electrochemical performance. The pressurized methane conversion kinetics and the increase in equilibrium methane concentration are considered in a new rate expression. The models were then applied in simulations to predict how the distributions of direct internal reforming rate, temperature, and current density are effected within stacks operating at elevated pressure. A generic 10 cm counter-flow stack model was created and used for the simulations of pressurized operation. The predictions showed improved thermal and electrical performance with increased operating pressure. The average and maximum cell temperatures decreased by 3% (20 °C) while the cell voltage increased by 9% as the operating pressure was increased from 1 to 10 atm.

1. Introduction

The continuously increasing demand for electrical power, high efficiency, and the reduction of green house gas emissions provides impetus for the creation of new power plant designs. Solid oxide fuel cell (SOFC) stacks, with their high power density and fuel flexibility, are prime candidates to serve as the building blocks for these power plants. Builders of SOFC stacks for power plant applications, seeking to maximize reliability and minimize cost and system complexity, are driven to design stacks of cells with increasingly large active areas (500 cm^2 and larger) and simplified manifolds and piping systems. Cells of larger size generate increased amounts of excess heat adding to the complexity of the thermal management of the stacks and systems. Excess heat from the electrochemical reactions increases proportionally to the active area (L^2) and the electrical power generated, while the pathways for removing heat from the stack scale with the cell edge length (L). Subsequently, as the stacks become larger and more powerful, the ability to remove excess heat becomes more challenging. With larger heat loads there is an increased risk of excessively high temperatures within the stack. Stable electrical and thermal–mechanical performance of the low-cost metallic interconnect materials (contact and sealing materials as well), depends strongly on the maximum temperature they experience under long-term operation [1,2]. Thus it is important to design for optimal heat transfer, maximize the cathode air flow for sensible heat cooling, and to make efforts to reduce the excess heat load within the stack.

Two methods of reducing the excess heat load are to increase the electrochemical efficiency, and to make use of direct internal reformation (DIR) cooling. The electrochemical efficiency of the SOFC is increased by pressurized operation. The increased efficiency caused by pressurization is due to increased chemical and electrical potential resulting in increased operating voltage (and output power), which subsequently decreases excess heat from the electrochemical reactions. Pressurization of the SOFC is a viable option when coupled with a compressor and expander in an integrated coal gasification fuel cell (IGFC) power plant with carbon capture [3].

DIR cooling refers to the process by which methane in the fuel stream is reformed with steam in the anode to generate hydrogen and remove heat directly from the electrochemical reactions. The enhanced efficiency of pressurized electrochemistry and the substantial heat load reduction available with DIR show promise for assisting in the effective thermal management of large SOFC stacks.

Modeling of pressurized SOFC systems in the literature include work by Aguiar et al. [4] to optimize a combined pre-reformer/internal reforming SOFC to achieve an auto-thermal system, and Dokamaingam et al. [5] examined the reforming activity of an indirect internal reformer, and the reformer/fuel cell was

* Corresponding author. Tel.: +1 509 372 4840; fax: +1 509 375 3865.
E-mail address: kp.recknagle@pnl.gov (K.P. Recknagle).

0378-7753/$ – see front matter © 2010 Published by Elsevier B.V.
doi:10.1016/j.jpowsour.2010.04.024

pressurized to achieve improved system efficiency. Another group (Onda et al. [6]) examined the power and efficiency of an SOFC-gas turbine cycle, with external and indirect internal reformers, as a function of operating pressure and feed gas recirculation. This paper is focused on the direct internal reforming (DIR) SOFC, investigates the effect of pressurization on the electrochemistry and steam-reforming reaction, and provides a new model that characterizes the combined effects. The model is then applied to simulations of a generic counter-flow stack operating on methane-rich fuel under pressurized and non-pressurized conditions as an example of the spatial and overall effects on performance.

2. Atmospheric electrochemistry and reforming

For the SOFC, the ideal equilibrium open circuit potential is due to the difference in chemical potential between the cathode–electrolyte and anode–electrolyte interfaces. This is the Nernst potential which can be expressed as a function of the partial pressure of oxygen (P_{O_2}) at the anode–electrolyte and cathode–electrolyte interfaces:

$$V_{Nernst} = \frac{RT}{4F} \ln \left(\frac{P_{O_{2,cathode}}}{P_{O_{2,anode}}} \right) \quad (1)$$

Here R is the universal gas constant ($8.3145\,\mathrm{J\,mol^{-1}\,K^{-1}}$), T is the temperature in Kelvin, and F is Faraday's constant ($96{,}485\,\mathrm{A\,s\,mol^{-1}}$). This chemical potential causes the reduction of oxygen in the cathode (Eq. (2)), and the oxidation of hydrogen in the anode (Eq. (3)), converting chemical energy to electrical energy.

$$\tfrac{1}{2}O_2 + 2e^- \rightarrow O^{2-} \quad (2)$$

$$H_2 + O^{2-} \leftrightarrow H_2O + 2e^- \quad (3)$$

Overall the global exothermic electrochemical reaction is:

$$H_2 + \tfrac{1}{2}O_2 \rightarrow H_2O + 2e^- \quad \Delta H_{298} = -242\,\mathrm{kJ\ mol^{-1}} \quad (4)$$

When the external circuit of the SOFC is closed, an electrical current is generated based on the rate at which hydrogen is electrochemically consumed. Voltage losses are introduced with the generation of current in the SOFC. These losses detract from the Nernst potential to yield the net cell voltage. There are three main losses in an SOFC: activation polarization, concentration polarization and ohmic losses. At low current densities, the electrochemical activation polarization losses are the dominant loss mechanism. At intermediate current densities the over-potentials are dominated by ohmic losses within the stack components. As the current density increases further, concentration polarization resulting from the build-up of reactant and product gases in the electrodes causes additional losses. These three losses are described using a current–voltage (I–V) relation for the local conditions of the SOFC in terms of effective cell properties and operational parameters. The I–V relation is specific for the materials, gas compositions, pressure, and temperature of a given cell [7,8] and is used to determine the voltage of the fuel cell as:

$$V(i) = V_{Nernst} - iR_i - \eta_{act,e} - V_{cath} - V_{anode} \quad (5)$$

where iR_i is the sum total of the temperature dependent ohmic losses of the electrodes, electrolyte, and interconnections within the stack, $\eta_{act,e}$ is the electrode (anode and cathode) activation polarization, and V_{cath} and V_{anode} are the electrode concentration polarizations, which depend on the porosity, tortuosity and thickness of the electrodes, gas diffusivity, temperature, and current density [9]. Increased electrode thickness or tortuosity will increase the concentration polarization.

The activation polarization ($\eta_{act,e}$) is controlled by the electrode reaction kinetics and represents the voltage loss incurred due to initiating charge transfer. It is related to the exchange current density (i_0) by the phenomenological Bulter–Volmer (B–V) equation [10] describing the charge transfer rate for the global electrochemical reaction (Eq. (4)):

$$i = i_0 \frac{RT}{(2+\alpha_e)F} \left[\exp\left(\frac{2F\eta_{act,e}}{RT} \right) - \exp\left(\frac{-\alpha_e F \eta_{act,e}}{RT} \right) \right] \quad (6)$$

where α_e is the charge transfer coefficient, which for the SOFC is 1 and 2 for the anode and cathode, respectively.

3. Steam–methane reforming

Steam–methane reforming occurs on the surface of a catalyst, such as the nickel in the Ni–YSZ anode of the SOFC. The methane combined with steam is converted to hydrogen and carbon monoxide by the endothermic steam–methane reforming reaction (Eq. (7)). In conjunction with the reformation is the water-gas shift (WGS) reaction (Eq. (8)), which rapidly equilibrates throughout the anode.

$$CH_4 + H_2O \underset{k_{rb}}{\overset{k_{rf}}{\leftrightarrow}} 3H_2 + CO \quad \Delta H_{298} = 206\,\mathrm{kJ\ mol^{-1}}$$

(forward reaction) (7)

$$CO + H_2O \underset{k_{sb}}{\overset{k_{sf}}{\leftrightarrow}} H_2 + CO_2 \quad \Delta H_{298} = -41.1\,\mathrm{kJ\ mol^{-1}}$$

(forward reaction) (8)

According to much of the literature for steam reforming of methane over a nickel catalyst, including tests at pressures up to 41 atm, the conversion rate is first order, or nearly first order in methane as reviewed by Lee et al. [11] and as corroborated by their own tests. The review also revealed there is little consensus about the dependence of the reaction rate on steam partial pressures due in part to differences in catalyst activities and the range of conditions tested by the investigations. Some testing at atmospheric pressure [11–13], and at very low pressures (0–10 Torr) [14] showed negative steam reaction order. In the review [11], rate expressions were provided for seven of the investigations that were performed at total pressures ranging from 1 to 41 atm, two of which included zero steam dependence, while the remaining five showed steam reaction orders of 1 or greater. Some of the reviewed rate expressions with positive steam reaction orders have been used successfully in modeling investigations including: the development of DIR anode materials by Saeki et al. [15], and dynamic simulation and control of an industrial steam reformer by Alatiqi and Meziou [16]. An interesting modeling analysis by Elnashaie et al. [17] showed that a reforming rate expression developed by Xu and Froment [18] and used by others [4,5] could express positive or negative effects of steam depending on the conditions. For total pressure up to 1 atm and high temperature ($T > 800\,^\circ\mathrm{C}$) the effect of steam could hinder the methane conversion, and for total pressures of 1–15 atm and lower temperature ($T < 800\,^\circ\mathrm{C}$) the effect of steam could result in an increased reforming rate.

Past modeling of DIR in SOFC stacks performed by this group [19] used a rate law, derived experimentally by Nakagawa et al. [20] under atmospheric pressure testing conditions. The rate law was first order in methane over the range of gas pressures and temperatures in which we were interested, particularly, in units of kPa, $5 \le CH_4 \le 15$, $10 \le H_2O \le 50$, and $10 \le H_2 \le 30$, and temperatures in Kelvin $975 \le T \le 1275$ for simulations dealing with a total pressure of 1 atm. Their testing was performed at S:C of at least 2:1 to prevent coking of the nickel anode catalyst, and with at least 5 kPa of hydrogen to activate the reaction and prevent deactivation of the catalyst by sintering. Our later modeling work [21–23] used an expression derived experimentally by King et al. [24]. The

expression is provided here for convenience:

$$-r_{CH_4} = 2.188 \times 10^8 \exp\left(-\frac{E_a}{RT}\right) C_{CH_4} C_{CO_2}^{-0.0134} \ \text{mol s}^{-1}\,\text{gmcat}^{-1} \quad (9)$$

where E_a is the activation energy (94,950 J mole^{-1}) and the C_i are gas concentrations (mole cm^{-3}). This rate expression is the result of tests performed under atmospheric conditions in a plug flow reactor (designed to minimize concentration and thermal gradients) using Ni–YSZ catalytic powder, and as other investigators have done, using S:C ≥ 2 and CH_4:H_2 ≥ 10 to prevent coking and deactivation of the catalyst. This expression is based on testing of highly active samples of a Ni–YSZ catalyst, which moved the reforming reaction (Eq. (7)) forward proportional to the methane concentration. With the above-mentioned pressures of water and hydrogen present during the tests, the conversion rate showed no dependence on those species. The testing did show a slight hindering effect due to the presence of CO_2 as is reflected in Eq. (9). The form of Eq. (9) represents the forward reforming reaction, and is most suitable for reforming conditions sufficiently far from equilibrium. As was the case with the previous rate expression used [20], application of Eq. (9) is limited to atmospheric pressure simulation cases, and sufficient steam must be present (S:C > 1) in the gas feed to support the forward steam-reforming reaction. For simulations involving steam–methane reforming at elevated operating pressures the applicability of Eq. (9) is surpassed, hence it must be replaced with a new expression to account for the effect of the increased pressure.

A characteristic of increased total pressure (on the steam–methane reforming reaction) is to increase the methane concentration as the gas seeks a lower potential energy state (and lower gas volume) as the reverse reaction is favored and Eq. (7) is driven the left. Further discussion of this effect is included in Section 4.2 where a new reforming rate expression for high operating pressures is presented. The new rate expression is designed to provide similar rates as Eq. (9) for operation at atmospheric pressure at the same temperature and gas partial pressures, and to provide meaningful rates for operation at higher total gas pressures.

4. Pressurized electrochemistry and reforming

Models that characterize the effects of pressure on the electrochemistry and steam–methane reforming can be used to investigate and provide insight into the thermal and electrical performance changes that could be expected of a pressurized DIR–SOFC. Three-dimensional simulations of a DIR–SOFC stack operating at various pressures enable examination of spatial temperature and current density distribution changes, and the coupled electrical performance of the stack. Insights gained by such simulations can be of assistance when considering operational changes for existing systems and for designing new systems. To this end this paper presents a new pressurized electrochemistry and reforming (PER) model for simulating pressurized operation in a DIR–SOFC stack. The model includes a modified electrochemistry polarization term and a new reforming rate expression to account for the effects of operating the SOFC at high pressure on the fuel cell's performance.

4.1. Pressure effects on electrochemistry

When an SOFC is pressurized, the Nernst potential (Eq. (1)) will increase based on the partial pressure of oxygen at the electrode–electrolyte interfaces. Data collected during pressurized operation of tubular SOFCs at Siemens Westinghouse and summarized editorially by Singhal [25] showed that the increase in cell voltage was larger than that attributable to the increased Nernst potential alone. The additional performance improvement was thought to be a result of decreased activation and cathode concentration polarizations. Tubular, cathode supported SOFCs can have 1–2 mm thick cathodes and subsequently large cathode concentration polarizations [25].

Nagata et al. [10] modeled the Siemens pressurized tubular SOFC and showed a much larger contribution to the total polarization from the activation polarization than from the concentration polarization. In fact the combined anode and cathode concentration polarizations were less than the activation polarization of either electrode. A similar electrochemical performance model, developed by Iwata et al. [26] for the simulation of a planar, electrolyte supported SOFC, with a thin (35 μm) anode and cathode found the concentration polarization to be much smaller in magnitude than the anode and cathode activation polarizations. The PER model includes the concentration polarizations for operation at atmospheric conditions [9] and considers the effect of pressurization on the activation polarizations in both the anode and the cathode.

The activation polarization is independent of the electrode thickness and, as found by Sawata et al. [27] depends upon the electrode–electrolyte interface conductivity and the exchange current density. Nagata et al. [10] proposed a simplified exchange current density which is a function of the partial pressure of oxygen ($P_{O_{2,el}}$):

$$i_0 = \beta_{act} \ \exp\left(\frac{-E_{act}}{RT}\right) P_{O_{2,el}}^{\gamma} \quad (10)$$

where β_{act} is a constant, γ is the reaction order, and E_{act} is the activation energy. The reaction order for the cathode was found to be 0.5, while that of the anode was found to be 0.133 [10]. These reaction orders were corroborated by Iwata et al. [26] who used values of 0.5 and 0.15 for the cathode and anode, respectively. The pre-exponential β_{act} and activation energy $E_{act,e}$ can be viewed as adjustable parameters set to characterize a particular electrode performance. Eq. (10) is used to calculate the exchange current density in the PER model for the activation polarization in both the fuel and the air electrodes.

The PER model can be fit to contemporary and historical cell performance data for the purpose of validation and stack simulations. Fig. 1 shows the model applied to non-reforming (no methane in fuel) cases of constant fuel utilization tubular SOFC (cathode supported) data [25] as shown in Fig. 1a, and to planar SOFC (anode supported) data [28] as in Fig. 1b. While these two data sets do not represent contemporary, high-performance pressurization data, they do demonstrate the flexibility and suitability of the model for application to general pressurized SOFC performance.

4.2. Pressure effects on direct internal methane reforming

In addition to the effect on electrochemistry, pressurization effects the rate of the steam–methane reforming reaction (Eq. (7)), which for the DIR–SOFC occurs on the nickel surface in the Ni–YSZ anode. At high temperatures and low pressures the reaction kinetics drive the reforming reaction forward; while at low temperature and high pressure the reverse reaction is favored wherein, by the law-of-mass-action, the number of gas molecules (volume) and pressure will be minimized at equilibrium. To illustrate the effect of pressure and temperature on the steam–methane reforming reaction, the commercially available and validated chemistry code HSC Chemistry 5.1 [29] was used to calculate equilibrium gas compositions (based on an arbitrary input gas mixture of H_2, H_2O, CO, CO_2, and CH_4) for pressures ranging from 1 to 10 atm, and for temperatures from 650 to 850 °C. The methane concentration increased (Fig. 2a), and the hydrogen concentration decreased (Fig. 2b) with increasing pressure at any given temperature. Also, as the tem-

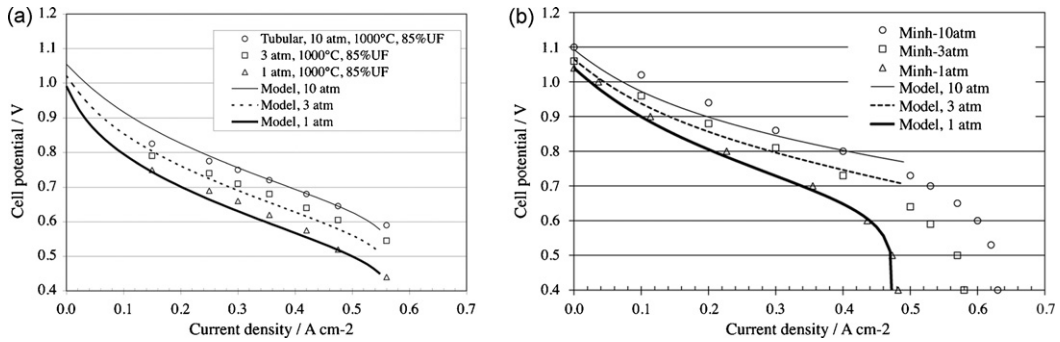

Fig. 1. The PER model fit to pressurized, non-reforming, electrochemical performance data of (a) tubular cell operating on 89% H_2, 3% H_2O, running at 1, 3, and 10 atm at constant 85% UF, and (b) planar cell operating on 25% H_2, 3% H_2O, running at 1, 3, and 10 atm.

perature increased, the forward reforming reaction is favored and the methane concentrations decrease at any given pressure. Our new reforming rate expression for use in elevated pressure applications includes these characteristic effects of pressurization and temperature on the steam–methane reforming reaction as described by the law-of-mass-action. According to the mass-action law, the rate of reaction of methane reformation can be expressed as the difference of forward and backward reactions (of Eq. (7)):

$$-r_{CH_4} = k_f \ \exp\left(-\frac{E_{af}}{RT}\right) p_{CH_4} p_{H_2O} - k_b \ \exp\left(-\frac{E_{ab}}{RT}\right) p_{CO} p_{H_2}^3 \quad (11)$$

where P_i are the gas partial pressures, and k_r and E_{ar} are forward and backward rate constants and activation energies, respectively. This expression is first order in methane, which suits the atmospheric pressure case, and is also first order in steam. Lehnert et al. [30] extracted kinetics models from testing data, and used one-dimensional anode diffusion and permeation gas transport models, with electrochemical reaction boundary conditions at the anode–electrolyte interface, to examine the effect of pressure distributions within the anode on the steam–methane reforming rate. From their results they arrived at the same form (as Eq. (11)) for their rate expression. Other modeling investigations have also used rate expressions originating from the law-of-mass-action to describe pressurized reforming data [15,16].

At equilibrium the forward and backward rates of Eq. (11) are equal yielding:

$$\frac{k_f \ \exp(-E_{af}/RT)}{k_b \ \exp(-E_{ab}/RT)} = \left(\frac{p_{CO} p_{H_2}^3}{p_{CH_4} p_{H_2O}}\right)_{eq} = K_{eq} \quad (12)$$

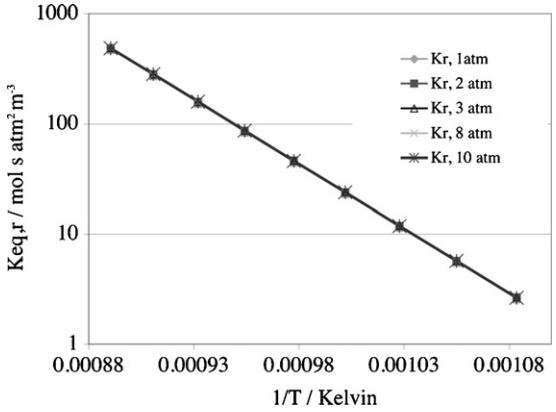

Fig. 3. Equilibrium constant for the steam–methane reformation reaction for pressures of 1–10 atm and temperatures from 650 to 850 °C. The solid line is calculated from Eq. (14).

The equilibrium constant is defined as

$$K_{eq,r} = \exp\left(-\frac{\Delta_r G^0}{RT}\right) \quad (13)$$

The equilibrium concentration data shown graphically in Fig. 2a and b were used to calculate the equilibrium constant via Eq. (12) over the given range of temperatures and pressures. Fig. 3 shows that the equilibrium constant for all pressure cases overlay each other demonstrating that the equilibrium constant is independent of the pressure, and that the temperature dependence is fit by an Arrhenius expression consistent with Eq. (13). The forward reaction activation energy (E_{af}) is provided by the previous rate expression (Eq. (9)) and the backward reaction activation energy depends upon the Gibbs free energy of the reaction ($\Delta_r G^0$) and the forward

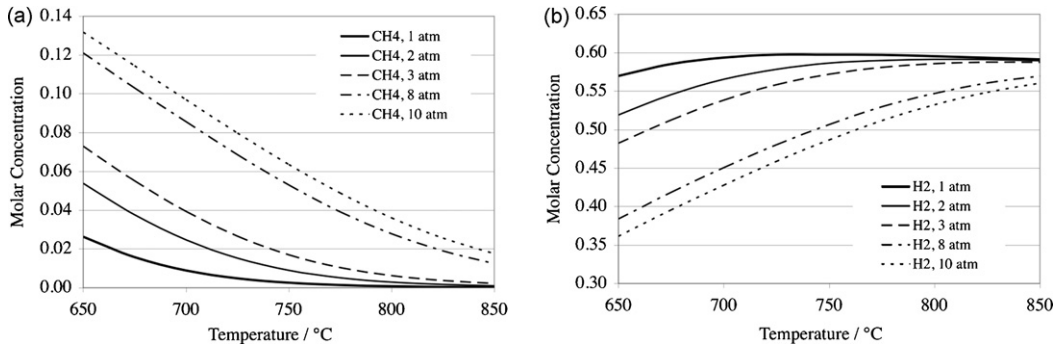

Fig. 2. Equilibrium molar concentrations of (a) methane and (b) hydrogen based on an arbitrary input gas mixture of H_2, H_2O, CO, CO_2, and CH_4.

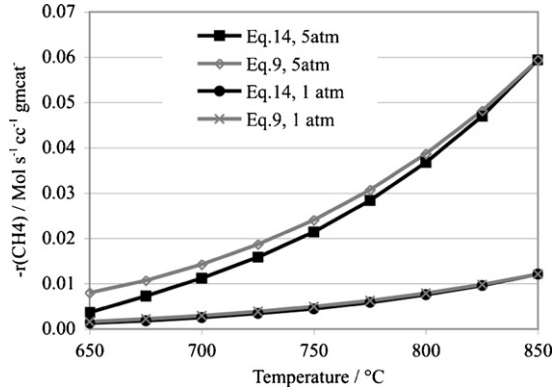

Fig. 4. Steam–methane reforming rates for a non-equilibrium gas with composition: 11% CH_4, 33% H_2O, 5% CO, 33% H_2, 6% CO_2, and 12% N_2.

reaction rate constant according to Eq. (12). Thus combining Eqs. (11)–(13) yields the final rate expression:

$$-r_{CH_4} = k_f \exp\left(-\frac{E_{af}}{RT}\right)\left[p_{CH_4}p_{H_2O} - \frac{p_{CO}p_{H_2}^3}{K_{eq}}\right] \quad (\mathrm{mol\,s^{-1}\,gmcat^{-1}}) \tag{14}$$

This new rate expression drops the nearly zero CO_2 dependence of Eq. (9), while maintaining thermodynamic consistency between forward and backward reactions necessary for conditions at or near equilibrium under which the reverse reaction can occur and the methane pressure will increase with increased pressure as shown in Fig. 2a. Choosing an appropriate value for k_f (9110 mol s^{-1} $gmcat^{-1}$ atm^2) Eq. (14) yields the same rate as the previous expression (Eq. (9)) at 800 °C. Fig. 4 compares steam–methane reforming rates calculated using the new (Eq. (14)) and previous (Eq. (9)) rate expressions for total pressures of 1 and 5 atm for a non-equilibrium gas with composition (11% CH_4, 33% H_2O, 5% CO, 33% H_2, 6% CO_2, and 12% N_2). At both 1 and 5 atm the rates are equal at 800 °C and the new rate is lower than the previous rate at lower temperatures (52% lower at 5 atm and 650 °C).

The reforming reaction is tightly coupled to the WGS reaction (Eq. (8)), which is assumed to be at equilibrium, resulting in:

$$K_{eq,s} = \left[\frac{P_{H_2O}P_{CO}}{P_{CO_2}P_{H_2}}\right]_{equil} = \exp\left(\frac{-(\Delta G^0_{CO} + \Delta G^0_{H_2O} - \Delta G^0_{CO_2})}{RT}\right) \tag{15}$$

where

$$\Delta G^0_k = \Delta H^0_k + A_k T \ \log T + B_k T^2 + C_k T^{-1} + D_k T \tag{16}$$

and $A_k - D_k$ are fitted parameters [31]. For implementation of the model into the simulation code, the WGS reaction rate (R_s) is chosen iteratively such that equilibrium (Eq. (15)) is satisfied.

5. Stack channel simulations

The PER model discussed in Sections 4.1 and 4.2 can be applied directly to examine the behavior of an SOFC test specimen with a very small active area over which current density, temperature, gas concentrations, and other scalars can be considered uniform. Within a planar cell or stack, of substantial active area (e.g. 100 cm^2 or larger), these scalars can have substantial variations and cannot be considered uniform. Thus, when designing a large stack it is useful to examine these spatial variations with model predictions to determine how they can be expected to affect the performance [21–23,32–35]. To investigate the spatial variations of temperature, current and voltage, in SOFC stacks, the PER model was implemented in a general-purpose transport code in which three-dimensional model geometries can be created. Within user-defined subroutines hooked to the transport code, the PER model provides mass, species, and thermal source terms to couple the spatial thermal-fluid-electrochemical-chemical solutions.

Computations for the steady state thermal-fluid solutions were performed using a traditional formulation for conservation of mass, species, momentum, and energy [36],

$$\frac{\partial}{\partial x_j}(\rho \tilde{u}_j) = S_m \tag{17}$$

$$\frac{\partial}{\partial x_j}(\rho u_j Y_k + F_{k,j}) = S_k \tag{18}$$

$$\frac{\partial}{\partial x_j}(\rho \tilde{u}_j u_i - \tau_{ij}) = -\frac{\partial p}{\partial x_i} + S_p \tag{19}$$

$$\frac{\partial}{\partial x_j}(\rho \tilde{u}_j h) = \frac{\partial}{\partial x_j}(\tilde{u}_j p) - p\frac{\partial u_j}{\partial x_j} + \tau_{ij}\frac{\partial u_i}{\partial x_j} + S_h \tag{20}$$

where the x_j are the Cartesian coordinates ($j = 1, 2, 3$), u_j is the fluid velocity components in direction x_j, p is the pressure, ρ is the gas density, Y_k is the gas specie mass fraction, $F_{k,j}$ is the gas diffusional flux component and S_m, S_k, S_p, and S_h are mass, species, momentum, and enthalpy source terms, respectively. The mass source term (S_m) in Eq. (17) accounts for mass transport of oxide ions through the electrolyte while the species source terms (S_k) in Eq. (18) account for the consumption of O_2 and H_2, and the generation of H_2O at the interfaces of the electrolyte with the cathode and anode, as well as the other reforming, and shift reaction species, CH_4, CO, and CO_2. The Faradic O_2 and H_2 species source terms, due to the electrochemical reactions, are proportional to the electrical current (Eq. (6)), which includes the effect of the pressurized Nernst potential (Eq. (1)) and the pressurized exchange current density (Eq. (10)), through Faraday's law:

$$s_{H_2,Faradic} = -\frac{i}{2F}, \quad s_{O_2,Faradic} = -\frac{i}{4F} \tag{21}$$

The gas species source terms (S_k) are completed by including the Faradic source terms, and the reformation (R_r) and shift reaction (R_s) rate sources terms. In the anode region they become:

$$s_{H_2} = s_{H_2,Faradic} + 3R_r + R_s \tag{22}$$

$$s_{H_2O} = -s_{H_2,Faradic} - R_r - R_s \tag{23}$$

$$s_{CH_4} = -R_r \tag{24}$$

$$s_{CO} = R_r - R_s \tag{25}$$

$$s_{C_2O} = R_s \tag{26}$$

and in the cathode air region the gas species source term is:

$$s_{O_2} = s_{O_2,Faradic} \tag{27}$$

Enthalpy released by the local electrochemical reaction (Eq. (4)), diminished by the electrical power, and modified by the local enthalpy of the methane reforming and WGS reactions provide the source term (S_h, W m^{-3} s^{-1}) for the thermal energy and temperature solution (Eq. (20)). For the simulations all equations were solved in an iterative and fully coupled solution.

5.1. Model geometry and boundary conditions

The geometry chosen for the model was a generic, modestly sized (10 cm in length) counter-flow stack channel with active area width of 5.42 mm. The 10 cm length was selected to provide sufficient dimensions for substantial spatial variations to exist. The three-dimensional model geometry is shown in partial view

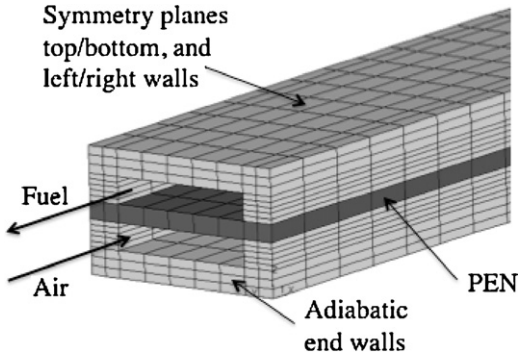

Fig. 5. Partial isometric view of three-dimensional channel model used for the simulations.

in Fig. 5. The model is composed of 10,268 computational elements and includes 1 mm tall fuel and air flow channels and a 0.66 mm thick membrane-electrode assembly (MEA). Within the MEA, the anode, dense electrolyte, and cathode thicknesses are 600, 10, and 50 μm, respectively, and both electrodes have a 30% porosity and tortuosity factors of 2.5. Additionally, 2 mm thick separator/interconnect plates, and 1.21 mm (half thickness) ribs provide the interconnection from cell to current collector in the model. Within the active area the computational grid consisted of 5 elements across the channel, and 50 elements along the 10 cm length. For the application of planar SOFC stack simulations the number of computational elements required to model the cells, bipolar plates, and other components can become quite large. In general the distributions of temperature, current density, and gas species vary across the plane of each cell throughout the stack height, and the planar and macroscopic three-dimensional distributions are of primary interest when examining the stack performance. For these reasons the present model does not resolve the temperature, charge density, or gas/surface/bulk specie distributions throughout the MEA thickness, instead it uses a single computational element through the MEA and calculates a single bulk temperature for that incremental portion of the planar cell. This is a suitable practice that this group has utilized in the past, and a description of the stack modeling methodology can be found in Recknagle et al. [37]. The model geometry as described was constructed to represent a single repeating channel unit located at the mid-level of a large, multiple-cell stack where thermal gradients between adjacent channels would be small and the gradients would be confined along the channel length; thus symmetry boundaries were used at the top, bottom, and side surfaces of the model to represent this condition, while adiabatic boundaries were used at the channel ends. Constant mass and constant temperature inflow boundaries were used for the air and fuel streams for simulations of constant current density (and constant fuel utilization) cases.

Table 1
Coefficients to give activation polarizations.

Location	α	β	E_{act}, kJ mol^{-1}	γ
Cathode	2	5.77E+05	125	0.5
Anode	1	7.0E+07	110	0.133

5.2. Fuel composition and electrochemical performance

For the present analysis the fuel was assumed to be gasified coal, the composition of which depends in part upon the gasifier type used. Hydrogen compositions can range from about 30% to over 50% depending upon subjection of the syngas to water-gas shift, CO_2 removal, hydrogen separation, and desulphurization processes [38,39]. Many of these processes result in fuel compositions containing very little methane. For large stacks whose maximum temperatures can become very large [23] reformation cooling is desirable to decrease the net heat load, and could have a positive effect on the temperature distribution within the stack. The feed gas was assumed to be methanized and delivered to the anode with the composition: 33% H_2, 33% H_2O, 5% CO, 6% CO_2, 11% CH_4, and 12% N_2 for all simulations. The methane content in this fuel gas would provide substantial on-cell reformation cooling and enable the effect on performance to be examined. The electrochemical performance of the cell operating on fuel of this composition and under atmospheric pressure was taken to be 0.8 V at 0.434 A cm^{-2} to reflect contemporary high-performance cell data, in contrast to data shown in Fig. 1a and b. This performance corresponds to operating conditions of 750 °C, with 65 and 15% fuel and air utilizations, respectively. Table 1 summarizes the coefficients for Eqs. (6) and (10) used to calculate the activation polarizations in the PER model.

5.3. Simulation test cases

To demonstrate the PER model and show the potential benefit of pressurized operation, a set of simulations were performed in which the above-mentioned current density, fuel and air utilizations, and inflow gas temperature of 670 °C, were held constant for operating pressures of 1–10 atm. Fig. 6a provides a plot of the reforming rates near the fuel inlet side (at right in the figure) for each operating pressure case. Reforming rates were the highest near the fuel inlet where methane concentrations were highest, and the reforming rates increased with increasing operating pressure, which as discussed in Section 3 is as expected for the simulated conditions of high total pressure and intermediate temperatures (≤ about 800 °C). The 1 atm case had a maximum reforming rate of 1.5E−07 mol m^{-3} s^{-1} and decreased to about zero within 2 cm as

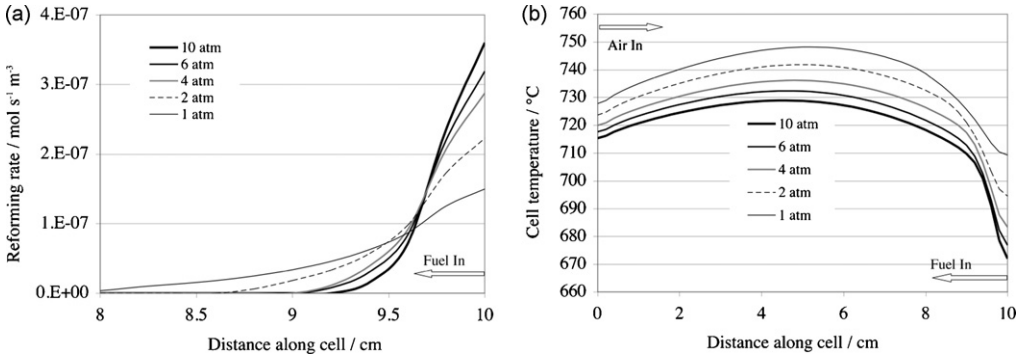

Fig. 6. Pressurized stack simulation results for internal reforming, operating pressures of 1–10 atm, and profiles of (a) methane reforming rate, mol m^{-3} s^{-1} and (b) cell temperature, °C.

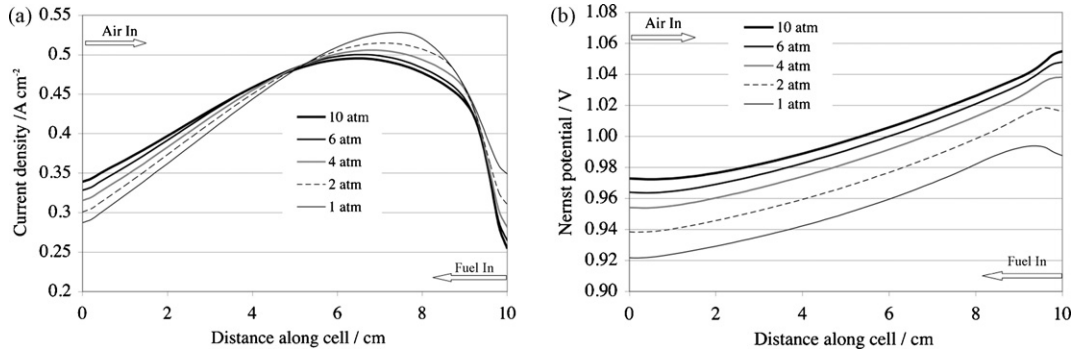

Fig. 7. Pressurized stack simulation results for internal reforming, operating pressures of 1–10 atm, and profiles of (a) current density, A cm^{-2} and (b) Nernst potential, V.

the methane was rapidly consumed. The reforming rate increased and the reaction length decreased as the operating pressure was elevated from 1 to 10 atm. In the 10-atm case, the reforming rate at the fuel inlet was 3.5E−07 mol m^{-3} s^{-1}, with a steep decrease to about zero as the reaction zone was approximately 1 cm in length. Beyond the primary reaction zone along the remaining cell length, in the absence of substantial methane concentration, the forward and reverse reaction rates were approximately at equilibrium. The faster reforming rate due to pressurization increased the temperature depression at the fuel-in edge, as illustrated in Fig. 6b (at right), resulting in an increased difference between minimum and maximum temperatures along the cell (∼40 °C at 1 atm and ∼58 °C at 10 atm). The temperature decreased with increased operating pressure along the full cell length resulting in decreased average and maximum cell temperatures. In all cases the methane was fully reformed, thus heat removal due to reforming was the same for each case. The decreased average and maximum temperature was due to decreased heat load resulting from increased electrical performance.

The fuel utilization and average current density of each operating pressure case were constant as noted, yet the distribution of the current density was affected by the cell temperature as shown in Fig. 7a. The current density was lower at the fuel-in edge for the increased pressure cases due to lower leading edge temperatures. The lower mid-cell temperatures also resulted in decreased maximum current density values mid-cell. Because the current density was decreased at the inflow edge and at mid-cell, more hydrogen was available downstream, and the current density values increased approaching the air-in (fuel-out) edge (at left). Underlying these results the Nernst potential was increased with increased pressure and decreased temperature along the full cell length (Fig. 7b). As a result, the cell voltage was consistently increased with increased operating pressure, with values ranging from 0.8 V at 1 atm to nearly 0.87 V at 10 atm (Fig. 8) for an overall increase of 9%. Thus pressurized operation of this SOFC example stack with internal reforming resulted in decreased maximum and average cell temperature with increased electrical performance.

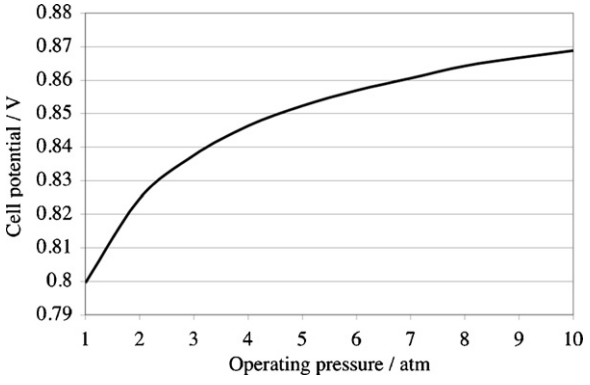

Fig. 8. Cell voltage versus operating pressure.

6. Conclusions

The constitutive pressurized electrochemistry and reforming (PER) model characterizing the pressurization effects has been applied to an existing SOFC performance model. The resulting electrochemistry model accounts for the SOFC performance due to increased Nernst potential and diminished activation polarization, both of which serve to boost cell voltage and power while lowering heat load and operating temperature. A rate expression for methane reforming that correctly considers the effects of pressure on the reaction kinetics, by the law-of-mass-action, allowing the methane concentration to increase with pressure at equilibrium was introduced. The PER model was implemented in a general-purpose transport code for simulations of pressurized DIR–SOFC stack operation at steady state. The iterative calculation procedure fully couples the thermal-fluid-electrochemical-chemical solution for meaningful predictions of DIR–SOFC stack performance trends. The capability was applied in simulations to evaluate the changes in spatial distributions of current density, temperature, and Nernst potential within a generic stack operating on methane-rich fuel and air at atmospheric and elevated pressures. The model predicted improved thermal and electrical performance in a 10-cm counter-flow stack with the operating pressure increased from 1 to 10 atm, as the average and maximum temperatures were decreased by 3% (20 °C), and the cell voltage increased by 9%.

Acknowledgements

The work summarized in this paper was funded as part of the Solid-State Energy Conversion Alliance Core Technology Program by the U.S. Department of Energy's National Energy Technology Laboratory. PNNL is operated by Battelle for the U.S. Department of Energy under Contract DE-AC05-76RL01830.

References

[1] S.P. Simner, M.D. Anderson, G.-G. Xia, Z. Yang, J.W. Stevenson, Ceram. Eng. Sci. Proc. 26 (4) (2005) 83–90.
[2] S.P. Simner, M.D. Anderson, G.-G. Xia, Z. Yang, V.L. Sprenkle, L.R. Pederson, J.W. Stevenson, J. Electrochem. Soc. 152 (4) (2005) A740–A745.
[3] K. Gerdes, E. Grol, D. Keairns, R. Newby, Integrated Gasification Fuel Cell Performance and Cost Assessment, 2009, DOE/NETL-2009/1361.
[4] P. Aguiar, D. Chadwick, L. Kershenbaum, Chem. Eng. Sci. 59 (2004) 87–97.
[5] P. Dokamaingam, S. Assabumrungrat, A. Soottitantawat, I. Sramala, N. Laosiripojana, Int. J. Hydrogen Energy 34 (2009) 410–421.
[6] K Onda, T. Iwanari, N. Miyauchi, K. Ito, T. Ohba, Y. Sakaki, S. Nagata, J. Electrochem. Soc. 150 (12) (2003) A1569–A1576.
[7] J.W. Kim, A.V. Virkar, K.Z. Fung, K. Metha, S. Singhal, J. Electrochem. Soc. 146 (1999) 69–78.

[8] L.A. Chick, J.W. Stevenson, K.D. Meinhardt, S.P. Simner, J.E. Jaffe, R.E. Williford, 2000 Fuel Cell Seminar, Abstracts, 2000, pp. 619–622.
[9] L.A. Chick, R.E. Williford, J.W. Stevenson, C.F. Windisch Jr., S.P. Simner, 2002 Fuel Cell Seminar, Palm Springs, CA, Abstracts, 2002.
[10] S. Nagata, A. Momma, T. Kato, Y. Kasuga, J. Power Sources 101 (2001) 60–71.
[11] A.L Lee, R.F. Zabranski, W.J. Huber, Ind. Eng. Chem. Res. 29 (1990) 766–773.
[12] A.L. Dicks, K.D. Pointon, A. Siddle, J. Power Sources 86 (2000) 523–530.
[13] J.R Rostrup-Neilsen, J. Catal. 31 (1973) 173–199.
[14] J.R. Ross, M.C.F. Steel, J. Chem. Soc., Faraday Trans. 69 (1) (1973) 10.
[15] M.J. Saeki, H. Uchida, M. Wantanabe, Catal. Lett. 26 (1994) 149–157.
[16] M. Alatiqi, A.M. Meziou, Comput. Chem. Eng. 15 (3) (1991) 147–155.
[17] S.S.E.H. Elnashaie, A.M. Adris, A.S. Al-Ubaid, M.A. Soliman, Chem. Eng. Sci. 45 (2) (1990) 491–501.
[18] J. Xu, G.F. Froment, AIChE J. 35 (1989) 88–96.
[19] K.P. Recknagle, P. Singh, L. Chick, M. Khaleel, Proceedings of the Fuel Cell 2004 Seminar, San Antonio, TX, 2004, PNNL-SA-43248.
[20] N. Nakagawa, H. Sagara, K. Kato, J. Power Sources 92 (1–2) (2001) 88–94.
[21] K.P. Recknagle, B.J. Koeppel, X. Sun, J.S. Vetrano, S.T. Yokuda, M.A. Khaleel, P. Singh, Proceedings of the 30th Fuel Cell Seminar, Honolulu, HI, 2006.
[22] K.P. Recknagle, S.T. Yokuda, D.T. Jarboe, M.A. Khaleel, P. Singh, Proceedings of the 29th International Conference on Advanced Ceramics and Composites, 2006.
[23] K.P. Recknagle, B.J. Koeppel, X. Sun, M.A. Khaleel, S.T. Yokuda, P. Singh, J. Electrochem. Soc. 5 (1) (2007) 357–361.
[24] D.L. King, Y. Wang, Y. Chin, Y. Lin, H. Roh, R. Romiarek, Presented at SECA Core Technology Program Review Meeting, Tampa, FL, January, 2005.
[25] S.C. Singhal, Solid State Ionics 135 (2000) 305–313.
[26] M Iwata, T. Hikosaka, M. Morita, T. Iwanari, K. Ito, K. Onda, Y. Sakaki, S. Nagata, Solid State Ionics 132 (2000) 297–308.
[27] A. Sawata, K. Tsuneyoshi, J. Mizusaki, H. Tagawa, Solid State Ionics 40/41 (1990) 415–420.
[28] N Minh, Proceedings of the Texas Hybrid Meeting, Galveston, TX, 2002.
[29] A. Roine, HSC Chemistry 5.1 Users Guide, Outokumpu Research Oy. Information Service, 2002, 02103-ORC-T http://www.outokumpu.com.
[30] W. Lehnert, J. Meusinger, F. Thom, J. Power Sources 87 (2000) 57–63.
[31] CRC Handbook of Chemistry and Physics, 50th ed. p. D-45.
[32] K.P. Recknagle, R.E. Williford, L.A. Chick, D.R. Rector, M.A. Khaleel, Proceedings of the Fuel Cell 2002 Seminar, Palm Springs, CA, 2002, PNNL-36977.
[33] K. Keegan, M.A. Khaleel, L.A. Chick, K.P. Recknagle, S. Simner, J. Deibler, Society of Automotive Engineers, Congress 2002 Proceedings, 2002, 2002-01-0413.
[34] K.P. Recknagle, R.E. Williford, L.A. Chick, D.R. Rector, M.A. Khaleel, J. Power Sources 113 (2003) 109–114.
[35] M.A. Khaleel, D.R. Rector, Z. Lin, K.I. Johnson, K.P. Recknagle, Int. J. Multiscale Comput. Eng. 3 (2005) 33–48, PNNL-SA-42792.
[36] F.M. White, Viscous Fluid Flow, 2nd ed., McGraw-Hill, Inc., 1991.
[37] K.P. Recknagle, R.E. Williford, L.A. Chick, D.R. Rector, M.A. Khaleel, J. Power Sources 4996 (2002) 1–6.
[38] R.S. Gemmen, J. Trembly, J. Power Sources 161 (2006) 1084–1095.
[39] A Pettniau, A. Orsini, C. Amorino, Second International Conference on Clean Coal Technologies for our Future, Castiadas, Sardinia, Italy, 2005.